Nanocellulose-Mediated Transition of Lithium-Rich Pseudo-Quaternary Metal Oxide Nanoparticles into Lithium Nickel Cobalt Manganese Oxide (NCM) Nanostructures

Peter M. Zehetmaier,[a] Florian Zoller,[b, c] Michael Beetz,[a] Maximilian A. Plaß,[a] Sebastian Häringer,[a] Bernhard Böller,[a] Markus Döblinger,[a] Thomas Bein,[a] and Dina Fattakhova-Rohlfing*[b, c]

Abstract: We report the syntheses of various compounds within the pseudo-quaternary system of the type $Li_wNi_xCo_yMn_zO_\delta$ ($\delta \leq 1$) (pre-NCMs). Four different compositions of this compound were realized as ultrasmall crystalline nanoparticles of 1–4 nm diameter using low-temperature solvothermal reaction conditions in *tert*-butanol at only 170 °C. All of the pre-NCMs crystallize in the rock-salt structure and their lithium content is between 20% and 30% with respect to the complete metal content. By adjusting the lithium content to 105% stoichiometry in the solvothermal reaction, the pre-NCMs can easily react to the respective Li $(Ni_xCo_yMn_z)O_2$ (NCM) nanoparticles. Furthermore, nanosized desert-rose structured NCMs were obtained after addition of nanocellulose during the synthesis. By using the mixed metal monoxides as precursor for the NCMs, cation mixing between lithium and nickel is favored and gets more pronounced with increasing nickel content. The cation mixing effect compromises good electrochemical capacity retention, but the desert-rose structure nevertheless enables enhanced stability at high power conditions, especially for NCM333.

1. Introduction

Oxide compounds of cobalt, nickel and manganese play an important role in electrochemical energy storage as positive electrodes (cathodes) for lithium ion batteries (LIBs). Thus, $LiCoO_2$ (LCO) is the first commercialized cathode material and it is still used in a considerable number of LIBs over a quarter of a century after market introduction in 1991.[1–3] LCO is attractive because of its theoretical capacity of about 140 mAh g^{-1} up to 4.2 V, the low self-discharge and good cycling performance. However, major drawbacks of this material are the high cost and toxicity of cobalt within LCO, as well as a moderate energy density.[3–9] In order to overcome these problems without compromising the advantages, much research has been conducted to substitute cobalt in the layered $LiMO_2$. Complete substitution of Co by Ni leads to $LiNiO_2$ (LNO) with, on the one hand, a similar specific capacity, a higher energy density and lower cost compared to LCO. On the other hand, LNO exhibits higher thermal instability and the Ni^{2+}-ions have the tendency to substitute Li^+-sites during synthesis and delithiation and consequently block the lithium ion diffusion pathways. Complete substitution with Mn leads to the low-cost layered $LiMnO_2$, which shows a high practical specific capacity of around 200 mAh g^{-1}. However, manganese compounds face structural instability problems due to Jahn-Teller distortion, as well as Mn dissolution, followed by a loss of active material and a low cyclability. The best strategy so far is the combination of different metals within the MO_2 layers of $LiMO_2$, resulting in Li $(Ni_xCo_yMn_z)O_2$ (NCM) compounds that increasingly gain importance as cathodes in advanced LIBs.[3,4,10–12]

Besides the high specific capacity and energy density, high power density (high charging rate) is another important requirement for the electrode materials in advanced LIBs. Control of morphology and in particular, nanoscaling are very efficient ways to boost the power density of electrode materials.[13–16] Reduction of the particle size of the active materials to the submicron region or even to tens of nanometers drastically shortens the diffusion path lengths of electrons as well as of lithium ions. This can lead to higher accessible capacities even at high charging or discharging rates. Moreover, active materials in the nanosize region are known to cushion the volume changes of structural changes and strains during the lithium insertion and extraction.

Submicron sized particles of $LiNi_{1/3}Co_{1/3}Mn_{1/3}O_2$ (NCM333) can be produced with different methods. Especially sol-gel,[17–19] modified Pechini,[20] plasma pyrolysis,[21] coprecipitation[22] and hydrothermal[23] approaches lead to particle sizes of over

[a] Dr. P. M. Zehetmaier, M. Beetz, M. A. Plaß, S. Häringer, B. Böller, Dr. M. Döblinger, Prof. Dr. T. Bein
Department of Chemistry and Center for NanoScience (CeNS)
Ludwig-Maximilians-Universität München (LMU Munich)
Butenandtstrasse 5–13 (E), 81377 Munich (Germany)

[b] F. Zoller, Prof. Dr. D. Fattakhova-Rohlfing
Forschungszentrum Jülich GmbH
Institute of Energy and Climate Research (IEK-1) Materials Synthesis and Processing
Wilhelm-Johnen-Straße, 52425 Jülich (Germany)
E-mail: d.fattakhova@fz-juelich.de

[c] F. Zoller, Prof. Dr. D. Fattakhova-Rohlfing
Faculty of Engineering and Center for Nanointegration Duisburg-Essen (CENIDE)
University of Duisburg-Essen
Lotharstraße 1, 47057 Duisburg (Germany)

100 nm after additional calcination steps at over 750 °C. The synthesis of smaller particles, which are expected to further increase the power density, is much more challenging. So far only a few groups have developed techniques to obtain NCM333 nanocrystals between 10 nm and 100 nm including hydrothermal,[24] reverse-microemulsion[25] and combustion[26] strategies.

In our previous publication we have described a novel approach to fabricate nanostructured and nanosized lithium cobalt oxide (LCO) cathode materials, which is based on the synthesis of lithium-rich rock salt type CoO nanoparticles ("pre-LCO") followed by the temperature-assisted transformation to the electrochemically active high temperature LCO (HT-LCO) phase.[16] The benefit of using pre-LCO nanoparticles as nanostructured building blocks are the slow kinetics of their phase transformation to HT-LCO, enabling to obtain much smaller HT-LCO nanocrystals after the subsequent calcination as compared to other reported approaches.[16] It is appealing to extend this approach to more complex Li-Ni-Co-Mn quaternary oxide structures to enable the fabrication of NCM cathodes with an optimized nanomorphology. Different pseudo-binary and pseudo-ternary monoxide compounds of the system Li-Ni-Co-Mn adopting rock-salt structure such as $Li_xCo_{1-x}O$,[27–32] $Li_xNi_{1-x}O$,[33–41] $Co_xNi_{1-x}O$,[42–47] $Mn_xNi_{1-x}O$,[48] $Mn_xCo_{1-x}O$[49] and $Li_xMn_yNi_zO$[50] are already described in literature. However, there are no reports on pseudo-quaternary rock-salt type $Li_wNi_xCo_yMn_zO_\delta$ ($\delta \leq 1$) (pre-NCM) so far. Here, we show for the first time the fabrication of dispersible crystalline pre-NCM particles of various compositions and in the size range of 1–4 nm via the tert-butanol solvothermal route that was already successfully used in the syntheses of various metal oxides.[13–16,47,51–57] These pre-NCM building blocks form, after a combustion step, the respective NCM nanoparticles ($LiNi_{1/3}Co_{1/3}Mn_{1/3}O_2$ (NCM333), $LiNi_{0.5}Co_{0.2}Mn_{0.3}O_2$ (NCM523), $LiNi_{0.6}Co_{0.1}Mn_{0.3}O_2$ (NCM613) and $LiNi_{0.8}Co_{0.1}Mn_{0.1}O_2$ (NCM811) intergrown in a desert-rose-like morphology.

2. Results and discussion

Lithium-rich rock salt-type nickel cobalt manganese oxide $Li_wNi_xCo_yMn_zO_\delta$ ($\delta \leq 1$) (pre-NCM) nanoparticles of different compositions were obtained in a tert-butanol solvothermal route that has been proven successful for the syntheses of numerous metal oxide nanoparticles of very small size.[13–15,47,52–57] In a typical synthesis, $Ni(OAc)_2$, $Co(OAc)_2$ and $Mn(acac)_2$ were mixed in the respective molar ratios to obtain the four different NCM materials. Afterwards, LiOiPr was added in slight excess to the transition metal precursors (TM) in a molar ratio of 1.05:1.00 Li:TM. The resulting mixture was suspended in tert-butanol and heated in sealed stainless steel autoclaves at 165 °C for 17 h.

XRD patterns of the as-prepared dried reaction products indicate the presence of undefined organic compounds detected as strong reflections at 5–15° 2ϑ (Figure S1 in supporting information) that are most presumably derived from not-fully reacted precursors. The lithium organic compounds can be easily removed by washing with ethanol. After the washing step the rock-salt phase and an additional side phase whose reflections can be assigned to Mn_3O_4 are detectable in the XRD patterns (Figure 1a). Inductively-coupled plasma optical emission spectroscopy (ICP-OES) analysis reveals that the stoichiometry of Ni, Co and Mn ions for all washed pre-NCM nanoparticles is practically the same as in the initial reaction mixture. However, the molar ratio of the sum of lithium to transition metals in the washed nanoparticles is in the range of 0.25 to 0.43, hence, significantly lower than in the reaction mixture. According to the results of ICP-OES and XRD analyses, the obtained pre-NCM products crystallize in a rock salt type structure with the composition of $Li_{0.30}Ni_{0.27}Co_{0.23}Mn_{0.20}O_\delta$ (pre-NCM333), $Li_{0.23}Ni_{0.40}Co_{0.17}Mn_{0.20}O_\delta$ (pre-NCM523), $Li_{0.25}Ni_{0.47}Co_{0.08}Mn_{0.20}O_\delta$ (pre-NCM613) and $Li_{0.22}Ni_{0.62}Co_{0.08}Mn_{0.08}O_\delta$ (pre-NCM811) (Table 1), with $\delta \leq 1$ indicating a possible oxygen substoichiometry that however could not be determined experimentally.

The results derived from ICP-OES concerning the compositions of the different materials and the molar ratios between Ni, Co and Mn are also confirmed by X-ray photoelectron spectroscopy (XPS) data for all of the washed pre-NCM nanoparticles. Furthermore, the $2p_{3/2}$ peaks of all three transition metals can be fitted with the respective peaks of $M(OH)_2$ according to Biesinger et al.,[58] confirming that all three metals are in the same oxidation state of +II (Figure 1c). Nevertheless, XPS cannot give evidence of Li, since Li is not directly detectable and does not distinctly affect the local electronic structure of Co and Ni.[28,40]

The phase purity of the obtained particles was characterized using Raman spectroscopy (Figure 1d), as well. For the pure binary metal oxides NiO, CoO and MnO crystallizing in the rock-salt structure only weak Raman scattering can be expected due to the high symmetry of their unit cells.[59,60] Surprisingly, the Raman spectra of all washed pre-NCM particles demonstrate strong and distinct signals. The presence of such signals can be explained only by formation of mixed Ni—Co—Mn compounds in

Table 1. Compositions of the as-prepared and the washed nanoparticles of pre-NCMs in comparison.

| Sample assignment	Stoichiometry in the reaction mixture according ICP-OES (Li:Ni:Co:Mn)	Phase and chemical composition of washed reaction products according to XRD and ICP-OES	Particle size according to XRD [nm]
pre-NCM333	1.06:0.32:0.35:0.33	$Li_{0.30}Ni_{0.27}Co_{0.23}Mn_{0.20}O_\delta$	1.5
pre-NCM523	1.11:0.48:0.22:0.30	$Li_{0.23}Ni_{0.40}Co_{0.17}Mn_{0.20}O_\delta$	1.4
pre-NCM613	1.06:0.60:0.11:0.29	$Li_{0.25}Ni_{0.47}Co_{0.08}Mn_{0.20}O_\delta$	1.3
pre-NCM811	1.08:0.79:0.11:0.10	$Li_{0.22}Ni_{0.62}Co_{0.08}Mn_{0.08}O_\delta$	1.9
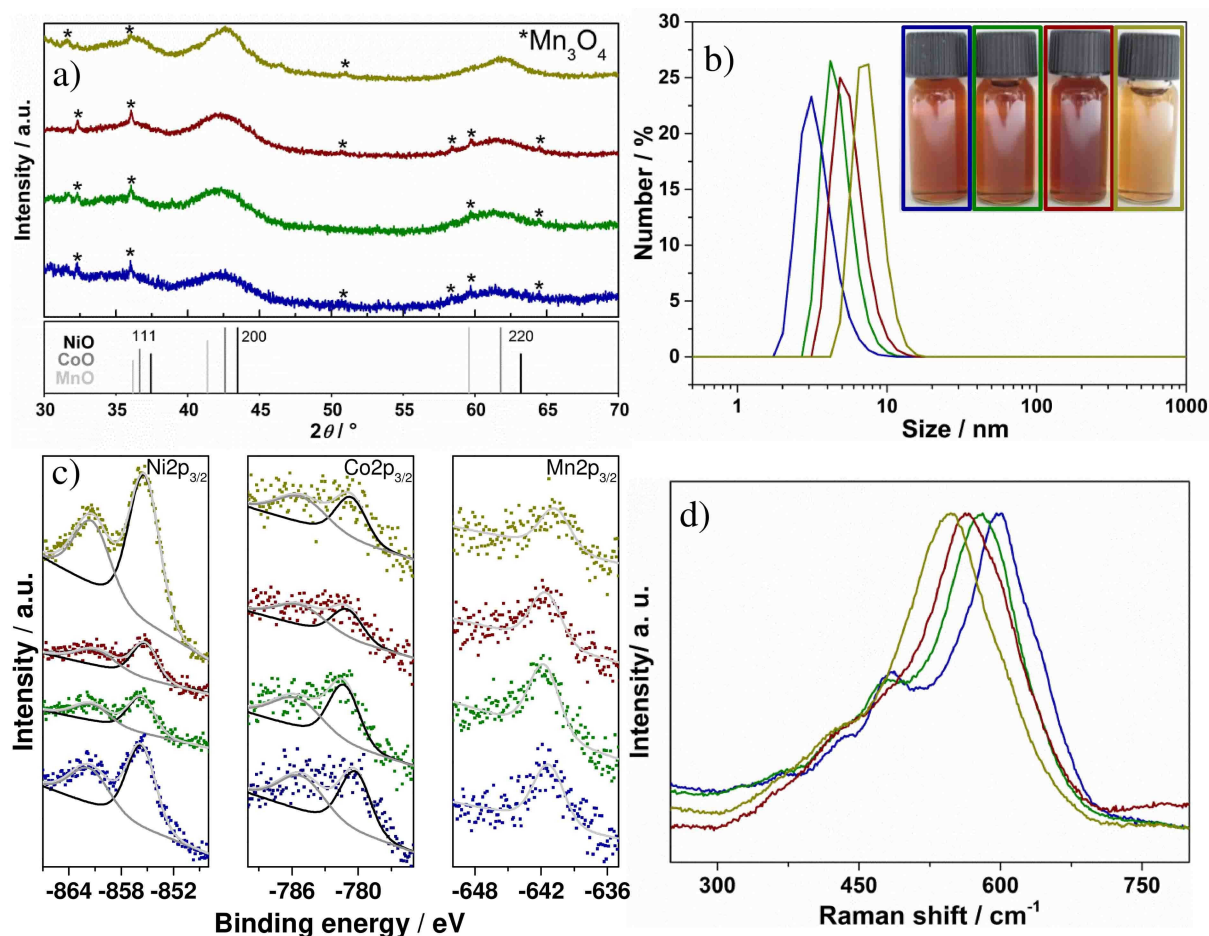
Figure 1. For all graphs the different pre-NCM materials are assigned the same colour: pre-NCM333 (blue), pre-NCM523 (green), pre-NCM613 (red) and pre-NCM811 (dark yellow): (a) XRD pattern of washed pre-NCM nanocrystals in comparison to ICDD card 00–001–1239 (NiO), ICDD card 00–001–1227 (CoO) and ICDD card 00–003–1145 (MnO). Impurities of Mn_3O_4 (ICDD card 00–001–1127) are indicated with stars. Fluorescence arising from measuring Co-containing samples with $CuK_{\alpha 1}$-radiation causes the background in the X-ray diffractogram. (b) DLS measurements of diluted dispersions in ethanol of the various pre-NCM. The insets show pictures of the respective dispersions at higher concentration. (c) XPS spectra of the Ni $2p_{3/2}$, Co $2p_{3/2}$ and Mn $2p_{3/2}$ peaks of the washed pre-NCM nanoparticles. (d) Raman spectra of pre-NCM nanoparticles.

which the symmetry is broken by the different neighbouring transition metals.[61] This assumption is further supported by the position of the most pronounced peak. In the literature this peak is referred to a first order one phonon (1P) longitudinal optical (LO) mode and is found to locate between 560 cm^{-1} and 570 cm^{-1} for NiO,[53,61,62] 530–560 cm^{-1} for CoO[16,59] and around 530–540 cm^{-1} for MnO.[60,63] For the pre-NCM333 the 1P LO mode is strongly red-shifted to 599 cm^{-1}, followed by 581 cm^{-1} for pre-NCM523, 563 cm^{-1} for pre-NCM613 and 547 cm^{-1} for pre-NCM811. It is known that the peak position can be significantly shifted by doping or substitution and is not just a superposition of the peaks in a pure physical mixture.[47,64] Moreover, the first order 1P transversal optical (TO) mode of NiO can be seen for all compositions in the region from 430 cm^{-1} for pre-NCM811 to 441 cm^{-1} for pre-NCM333.[60] We assume that the signals located around 480 cm^{-1} and only distinctly visible for pre-NCM333 and pre-NCM523 correspond to the 1P TO mode of CoO[59] and the signals around 370 cm^{-1} are assigned to the 1P TO mode of MnO.[60] Therefore, the

results of the Raman spectroscopy confirm the formation of a chemical mixture of the three transition metals and lithium within the single nanoparticles.

The mean size of the crystalline domains of pre-NCM particles corresponds to 1–2 nm as estimated from the broadening of the most pronounced (200) reflection in the XRD using the Scherrer equation. The particle size was also determined by using dynamic light scattering (DLS) on dispersions of the different pre-NCM materials (Figure 1b, inset). In order to obtain a homogenous dispersion, the particles were dissolved in ethanol and acetic acid. The latter is necessary to enhance the electrostatic repulsion of the individual particles. Interestingly, to stabilize these nanoparticles we needed the double amount of acetic acid in comparison to pure $Li_{0.15}Co_{0.85}O$ reported previously.[16] Additionally, for pre-NCM811 we even used four times the amount of acetic acid in comparison to the nickel-free oxide. This leads to the assumption that the nickel content influences the point of zero charge of the particles. With higher nickel content more acetic acid is required to fully disperse the

nanoparticles. The DLS data (Figure 1b) further confirm the higher tendency of agglomeration with increasing nickel content, as the hydrodynamic diameter rises. Pre-NCM333 shows, for example, a nanocrystal size in ethanol of 2–4 nm which is in accordance with the XRD-derived size. However, pre-NCM811 exhibits a size of 6–10 nm and this indicates a slight agglomeration of a few nanoparticles. Size analysis in scanning transmission electron microscopy in high angle annular dark field mode (STEM-HAADF) further confirms a size of 2–3 nm for all pre-NCM nanoparticles (Figure S2 in supporting information).

The morphology of the washed pre-NCM nanoparticles was investigated using STEM-HAADF (Figure 2). The electron diffraction patterns of all pre-NCM (insets in Figure 2b, d, f and h) can be indexed to the 111, 200 and 220 reflections typical for the cubic rock-salt structure.
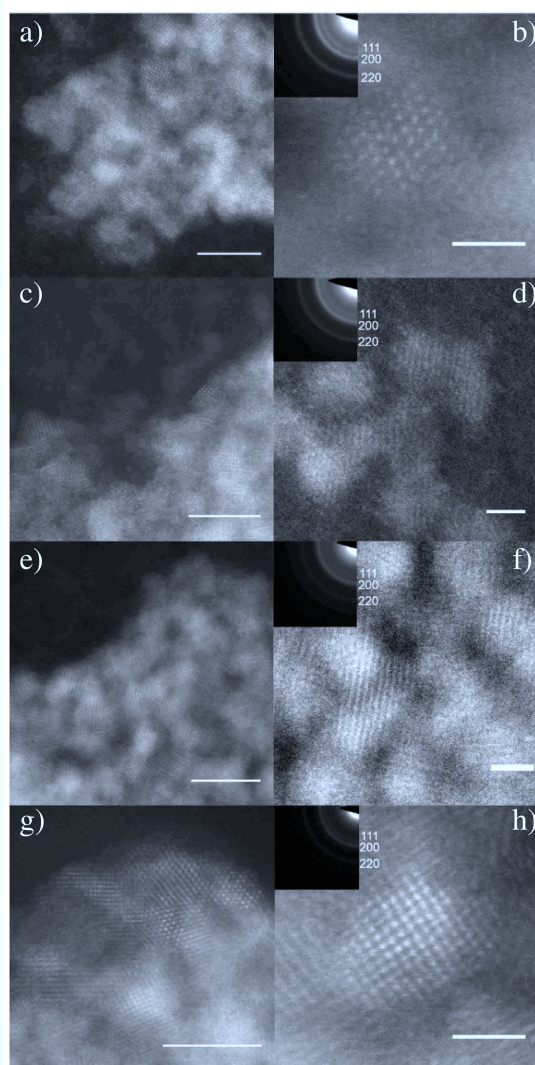

Figure 2. STEM-HAADF images of pre-NCM333 (a, b), pre-NCM523 (c, d), pre-NCM613 (e, f) and pre-NCM811 (g, h). Overview images with a scale bar of 5 nm (a, c, e, g) and single particles in detail with scale bar of 1.5 nm and the indicated electron diffraction pattern of the respective materials as insets (b, d, f, h).

In order to further confirm the results gathered from XPS and ICP-OES analysis, the compositions of the different washed pre-NCMs were determined by energy-dispersive X-ray spectroscopy (EDX) measurements, which were acquired during STEM-HAADF. Furthermore, the uniformity of the metal distribution in the particles was exemplarily investigated in case of the pre-NCM523 using EDX and electron energy loss spectroscopy (EELS) in STEM mode. While EDX was performed on areas larger than 100 nm × 100 nm, providing information about the average chemical composition, EELS was measured on very small areas down to single nanoparticles.

In Figure 3c, different element maps of Ni (Figure 3d), Co (Figure 3e) and Mn (Figure 3f) derived from EDX measurements are combined. It can be seen that for a major part of the sample, all elements are equally distributed and the transition metal stoichiometry of pre-NCM523 agrees well with that determined by other methods. It should be noted that although the element distribution is predominantly homogeneous throughout all samples, small regions with inhomogeneous elemental distributions have been observed as well. In Figure S3b in the supporting information, distinct bluish areas for Mn-rich parts, greenish areas for Co-rich parts and reddish areas for Ni-rich parts can be observed. EELS analysis of selected single nanoparticles confirms that the transition metal stoichiometry in each nanoparticle agrees with the average composition determined by ICP-OES, XPS and EDX. We have, however, observed minor variations in composition for individual nanoparticles. Thus, for six particles studied the Ni:Co:Mn ratio varies from 0.64:0.24:0.12 to 0.47:0.21:0.32, which is close to the expected composition within the measurement error of EELS.

The results of different characterization methods confirm that the solvothermal synthesis in *tert*-butanol leads to the formation of very small pre-NCM nanoparticles, whose composition can be described as a solid solution of NiO, CoO and MnO crystallizing in a rock salt structure with a homogeneous distribution of transition metal ions. Unfortunately, the accurate determination of the Li content within each nanoparticle remains challenging as none of the used methods enable an accurate determination of the Li content in the nanometer range. Quantification of Li with EELS is hardly possible as the $M_{2,3}$ edges of Ni, Co and Mn are in the same energy region as the K edge of Li.[65] Therefore, we can only determine an average Li content based on the results of ICP-OES analysis.

As mentioned above, one possible application of dispersible pre-NCM nanoparticles is their use as building blocks for nanostructured NCM cathode materials with tunable nanomorphologies for high power applications. As a suitable template for the nanostructure assembly we have tested nanocrystalline cellulose (NCC), a biogenic template that can be easily extracted from natural sources such as bacteria or cotton plants.[66,67] Besides being environmentally benign, the attractive features of NCC are its rod-like anisotropic shape (5–10 nm width and 100–300 nm length for cotton NCC) and the shape persistence, enabling the synthesis of different metal oxide motifs with a unique anisotropic nanomorphology.[67–72]
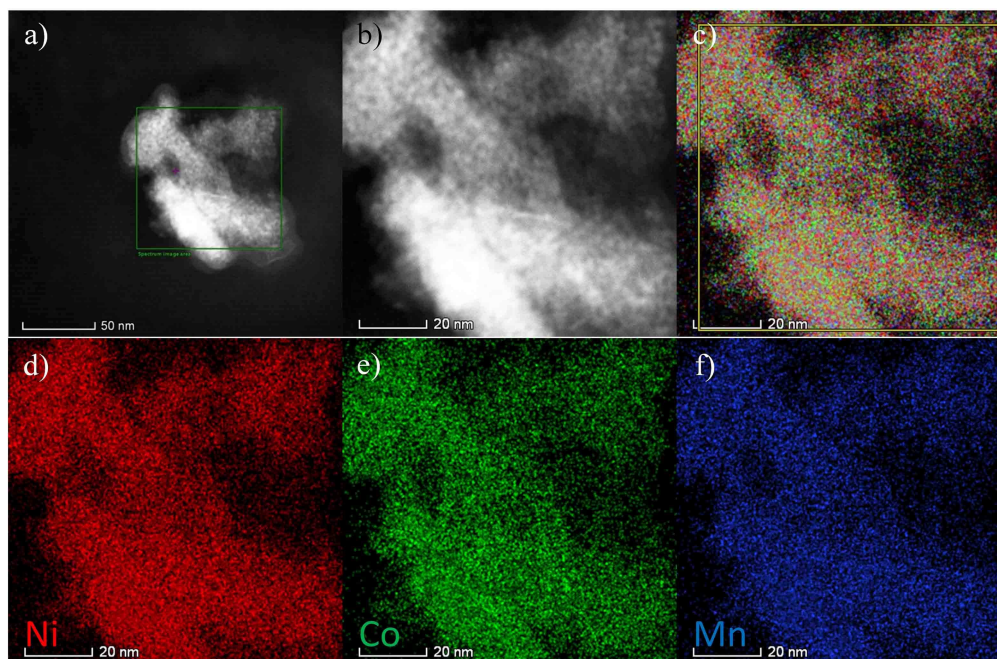
Figure 3. STEM-HAADF image of pre-NCM523 nanoparticles (a) including the selected area for the EDX acquisition (b). (c) Overlay of the detected Ni (d), Co (e) and Mn (f) EDX maps.

For the fabrication of electrochemically active nanostructured NCM, the as-prepared reaction product containing pre-NCM nanoparticles as well as non-reacted lithium compounds was filtered to remove remaining large aggregates, then diluted with water and finally mixed with a stock dispersion of the nanocellulose. The presence of an extra Li source is necessary to reach the right stoichiometry, as the amount of Li in pre-NCM nanoparticles is not sufficient for the formation of the targeted NCM phase. The weight ratio between the nanocellulose and the pre-NCM particles was taken as 1:1 and the overall nanocellulose concentration in the coating dispersion

was adjusted to be 0.8 wt%. The mixture was drop-cast on a glass substrate, dried at room temperature and calcined at 560 °C for 5 h. XRD patterns of the obtained products demonstrate that the calcination of cubic pre-NCM333 nanoparticles in the presence of nanocellulose results in the formation of hexagonal layered NCM333 (ICDD card 01–077–9286) crystallizing in the α-NaFeO$_2$ structure with space group R-3 m (Figure 4a).

Similar XRD patterns were also obtained for other pre-NCM compositions. While the 003 reflection remains at the same position for all NCM compositions indicating that the layers of
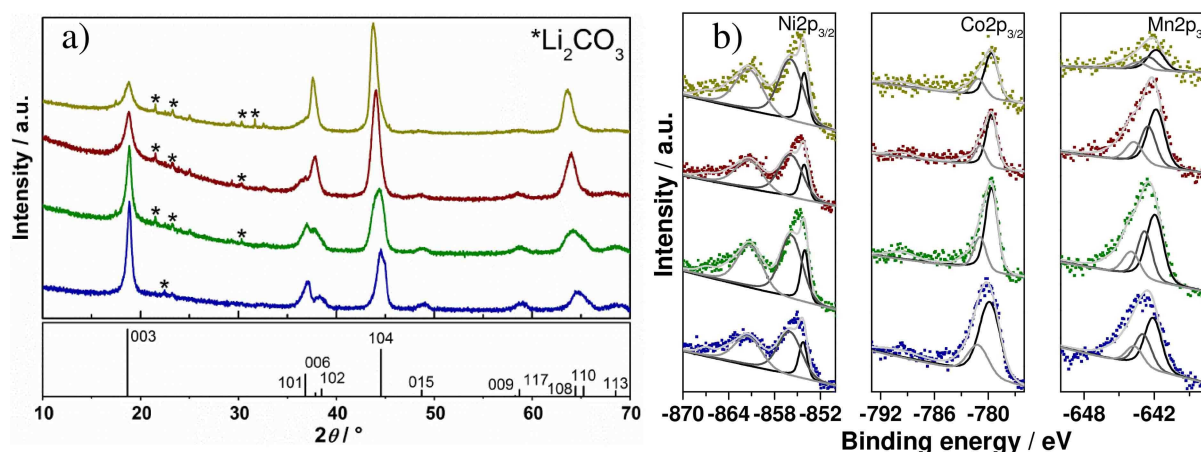

Figure 4. For all graphs, the different NCM materials are assigned the same color: NCM333 (blue), NCM523 (green), NCM613 (red) and NCM811 (dark yellow): (a) XRD of NCM nanocrystals in comparison of ICDD card 01–077–9286 of LiNi$_{0.33}$Co$_{0.33}$Mn$_{0.33}$O$_2$ (NCM333). Impurities of Li$_2$CO$_3$ (ICDD card 00–009–0359) are indicated with stars. (b) XPS of the Ni 2p$_{3/2}$, Co 2p$_{3/2}$ and Mn 2p$_{3/2}$ peaks on the NCM nanoparticles.

the hexagonal lattice have the same distance, the 104 reflection shifts to lower °2θ values for higher nickel content. One explanation for this could be that for higher Ni content more of the large Ni^{2+}-ions have to be incorporated into the crystal lattice of the α-$NaFeO_2$ structure, which leads to an expansion of the lattice and hence, to a shift to lower angles. Additionally, the 104 reflections of NCM333 and NCM523 seem to consist of two superimposed reflections of two structurally equivalent materials with different compositions, which will be discussed later in the context of the results obtained by EDX. The nanoparticle size can be calculated by using the Scherrer equation for the broadening of the 003 reflection. The result shows that with increasing Ni content the size of the nano-particles decreases from 19 nm for NCM333 over 16 nm for NCM523 and 11 nm NCM613 to 10 nm for NCM811.

ICP-OES analysis of different NCM compositions confirms that the stoichiometry of transition metal ions in the calcined samples is practically the same as in the pre-NCM nanoparticles, however, the total amount of lithium slightly decreases from 5% overstoichiometry to a nearly stoichiometric amount. Based on the results of ICP-OES analysis, the compositions of $LiNi_{0.33}Co_{0.33}Mn_{0.33}O_2$ (NCM333), $LiNi_{0.50}Co_{0.20}Mn_{0.30}O_2$ (NCM523), $LiNi_{0.60}Co_{0.10}Mn_{0.30}O_2$ (NCM613) and $LiNi_{0.50}Co_{0.20}Mn_{0.30}O_2$ (NCM523) for hexagonal NCM materials were obtained.

To unravel the nature of the individual transition metals in each compound XPS was used. For Ni, Co and Mn, their $2p_{3/2}$ peak (Figure 4b) was fitted with the corresponding reference spectra according to Biesinger et al.[58] For all compositions, the best fits were obtained for oxidation states of Ni^{2+}, Co^{3+} and Mn^{4+}. Ni was fitted with $Ni(OH)_2$ due to the surface adhering OH groups, Co with CoOOH, and Mn with MnO_2. For all different NCM compositions we found the same oxidation state (Ni^{2+}, Co^{3+}, Mn^{4+}) for each individual transition metal. Quantification with XPS confirmed the results already obtained with ICP-OES for the NCM compositions.

Scanning electron microscopy (SEM) images (Figure 5) demonstrate for each composition that the calcination of the self-assembly product of pre-NCM and nanocellulose results in the formation of an anisotropic desert-rose structure with intergrown walls perpendicular to the surface. The morphology of the different NCC-structured NCMs seems to vary depending on their composition. In case of a Co:Mn ratio of 1:1 (NCM333 and NCM811) the desert-rose structure is build up by large intergrown sheets, whereas with a decreasing ratio those sheets get smaller (Figure 5). In contrast to that, only dense nonporous material was obtained without using nanocellulose as a template (Figure S4 in supporting information).

Using nitrogen sorption experiments (Figure S5 in support-ing information) the BET-surfaces of the different structures can be determined. For the NCM333, NCM523, NCM613 and NCM811 samples, surface areas of 10 m^2g^{-1}, 11 m^2g^{-1}, 15 m^2g^{-1} and 13 m^2g^{-1}, respectively, were obtained. All BET surfaces are in the same range and small enough to not promote unfavourable side reactions as cathode material in LIBs. Furthermore, the pore size distributions (PSDs) derived from the individual isotherms by DFT calculations (Figure S5, insets) show a broad range of porosity for all NCM materials,
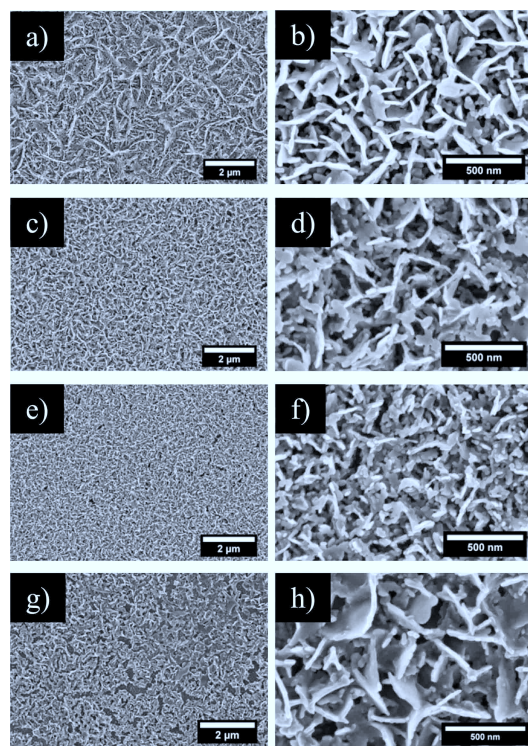

Figure 5. SEM micrographs of NCC-nanostructured NCM333 (a, b), NCM523 (c, d), NCM613 (e, f) and NCM811 (g, h) all exhibiting a desert-rose morphology. Overview images in low magnification (a, c, e, g) are shown in comparison to high-magnification micrographs (b, d, f, h).

from microporosity, due to textural porosity produced by agglomeration of the ultrasmall nanoparticles, to NCC induced meso- and macroporosity.

EDX analysis of different elements in SEM (Figure S6, Figure S7, Figure S8, Figure S9) reveal that the transition metal ions are uniformly distributed over large areas in a stoichiom-etry expected for the respective NCM materials within the error of EDX.

To investigate the structure and composition of each single nanoparticle, STEM-HAADF was performed. On the STEM micro-graphs of larger areas (Figure 6a, c, e, g) and of single nanoparticles (Figure 6b, d, f, h) for all compositions, the fine structure of the desert-rose morphology can be clearly seen and the diffraction patterns (insets in Figure 6b, d, f, h) of the respective areas prove that they are crystallized in the layered α-$NaFeO_2$ structure. For NCM333 and NCM523, however, square-like nanoplatelets (Figure S10) have also been observed in addition to the already mentioned rod-like morphology. Increasing Ni content generally leads to a smaller particle size (Figure S11). Thus, for NCM333 nanorods the average width and length is around 20 nm and 160 nm, respectively, for NCM523 12 nm×110 nm, for NCM613 13 nm×60 nm and for NCM811 10 nm×55 nm, respectively. The width of the nanorods is in a good approximation comparable to the sizes already derived from the XRD patterns. Compared to this, we found sizes for the nanoplatelets of 28 nm for NCM333 and 22 nm for NCM523 (Figure S12).
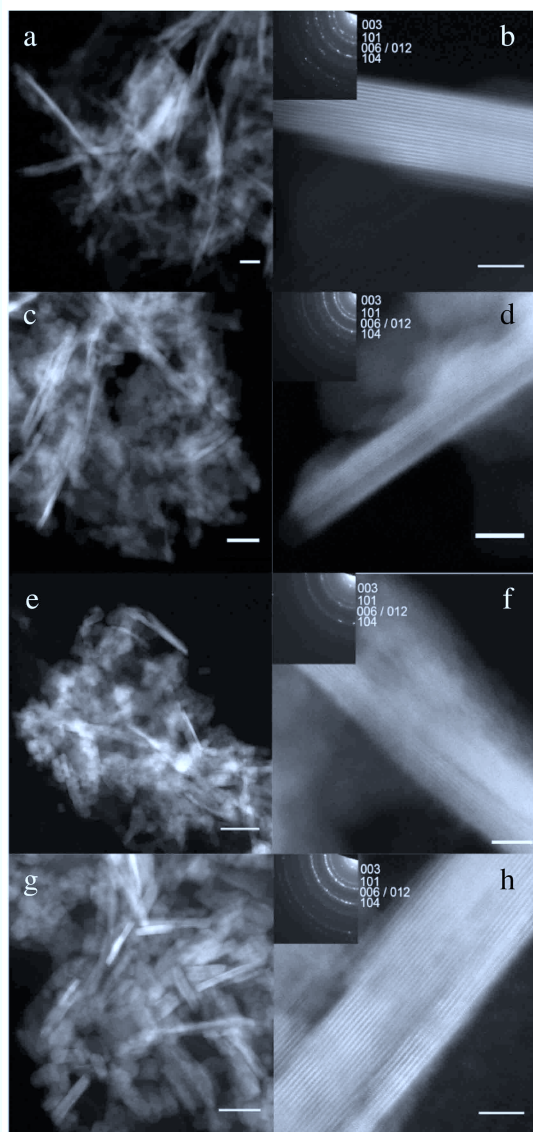
Figure 6. STEM-HAADF images of NCM333 (a, b), NCM523 (c, d), NCM613 (e, f) and NCM811 (g, h). Overview images of desert-rose agglomerates with a scale bar of 50 nm (a, c, e, g) and single rod-like nanoparticles in detail with scale bar of 5 nm, and the indicated electron diffraction pattern of the respective materials as insets (b, d, f, h).

In addition, ^{7}Li magic angle spinning nuclear magnetic resonance spectroscopy (MAS-NMR) was performed (Figure S13). All spectra of the NCMs show an unusually broad signal splitting of about 1400 ppm. The coupling of the unpaired electrons of Co^{2+}, Mn^{4+} and Ni^{2+} with Li^+ lead to the exceptionally broad spectrum.[16] This implies that Li^+ is coordinated by Co^{2+}, Mn^{4+} and Ni^{2+} ions which is in accordance with the α-$NaFeO_2$ crystal structure of NCM materials. Moreover, Raman spectroscopy was also performed on the material (Figure S14) and compared with the values reported in the literature for the Raman shifts of $LiNiO_2$,[73] $LiCoO_2$[74] and $LiMnO_2$.[75] Hereby, in a first approximation we assume that the Raman signal for the NCMs may derive from the superposition of the pure phases $LiNiO_2$, $LiCoO_2$ and $LiMnO_2$. Therefore, we are dealing with two peaks for the rhombohedral $LiNiO_2$ and $LiCoO_2$ (A_{1g} and E_g) and three signals, two A_g modes and one B_g mode, for the monoclinic layered $LiMnO_2$.[73–76] While the E_g band is not clearly visible as it overlaps with the A_{1g} peak, the latter can be determined for all NCMs. For NCM333 this peak is at 588 cm^{-1} and slightly decreases to 553 cm^{-1} with rising Ni content since the A_{1g} peak appears at 544 cm^{-1} for pure $LiNiO_2$.[73] Furthermore, for moderate Mn content, for NCM333, NCM523 and NCM613, the A_g mode is also visible at around 420 cm^{-1} as described in literature.[75]

In order to get insight into the phase transformation of pre-NCM nanoparticles to layered NCM in the presence of nanocellulose, we performed thermogravimetric analysis (TGA) and differential scanning calorimetry (DSC) analysis of the respective dry pre-NCM/nanocellulose mixtures (Figure S17 in supporting information). The combustion of pure nanocellulose is completed at temperatures as high as 534 °C (Figure S15 in supporting information). In contrast, it can be seen that the presence of pre-NCM significantly reduces the combustion temperature of the nanocellulose, which is also influenced by the relative fraction of Ni ions in the nanoparticles. Thus, the NCC is fully combusted already at 420 °C and 490 °C for the pre-NCM811/nanocellulose and the pre-NCM333/nanocellulose, respectively (Figure S17 in supporting information). Interestingly, the transformation of the pre-NCMs to the NCMs is completed much earlier than the full combustion of NCC. The transformation of the Ni-rich phases is completed again at lower temperatures (around 400 °C for pre-NCM811) than for Ni-poor pre-NCM333 (at 475 °C). Comparing the pre-NCM/nanocellulose composite with as-prepared pre-NCM, we can attribute the first major weight loss in the TGA diagrams at around 300 °C (Figure S16) to the oxidation of the pre-NCMs to NCMs, including the accompanying metal migration into the nanoparticles and the combustion of the residual precursor organics. The second large weight loss step at 400–450 °C can be assigned to the total combustion of NCC. Moreover, both processes occur already at lower temperatures compared to the separate processes in pre-NCM and pure NCC.

The addition of an extra Li source is necessary to reach the correct stoichiometry and to prevent the pre-NCM nanoparticles to form other phases (see Figure S18 in the supporting information). To illustrate this, after calcination at 560 °C for 5 h

Furthermore, the elemental compositions of the different morphologies were measured using EDX in STEM-mode. The nanorods were the only type of morphology found in NCM613 and NCM811 and they also showed the expected molar ratios for the different transition metals. For NCM333 and NCM523 however, the composition varied drastically between the two morphologies. While the nanoplatelet structures almost exhibited the estimated composition with around $LiNi_{0.25}Co_{0.40}Mn_{0.35}O_2$ for NCM333 and $LiNi_{0.48}Co_{0.22}Mn_{0.30}O_2$ for NCM523, the rod-like nanoparticles showed a lack of Ni and an excess of Co. The nanorods in NCM333 consisted in average of $LiNi_{0.13}Co_{0.60}Mn_{0.27}O_2$ and the ones in NCM523 of $LiNi_{0.15}Co_{0.48}Mn_{0.37}O_2$.

we observe the separation of the different transition metals under formation of their most stable oxide phases. Ni^{2+} still remains in NiO, while Co^{2+} is partly oxidized, thus forming Co_3O_4, and Mn^{2+} is fully oxidized, most likely forming $LiMn_2O_4$ or small amounts of MnO_2. To prevent this, we use in our dispersions the as-prepared pre-NCM powders with a slight overstoichiometric Li-content (as confirmed by ICP-OES).

Finally, the electrochemical properties of the NCMs were investigated by cyclic voltammetry. Cyclic voltammograms (CVs) of the cathodes containing the individual nanostructured NCMs (Figure S19a) feature oxidation and the respective reduction peaks at potentials around 3.6 V and 4.0 V typical for the Ni^{2+}/Ni^{4+} redox couple.[17,77] Furthermore, for all materials the first cycle exhibits a drastically higher current density than for the following cycles due to the formation of the cathodic solid-electrolyte interface (SEI). In contrast to the potential values of the redox peaks which remain practically the same for different NCM cathodes, the current densities differ significantly for different compositions. Thus, the current density of NCM333 is more than five times higher than that of the sample NCM811. The specific capacities obtained by the integration of the corresponding CV peaks also show a strong variation depending on the composition (Figure S19b). Thus, 70 mAh g^{-1} discharge capacity was obtained for NCM333, but only around 15 mAh g^{-1} for NCM811. These values are much lower than the expected values of 150–160 mAh g^{-1} for NCM333,[78] NCM523[79] and 203 mAh g^{-1} for NCM811,[80] respectively.

In literature two quality criteria for the NCM materials are currently used. The first is the ratio between the integrated intensities of the 003 to the 104 reflection I_{003}/I_{104} in X-ray diffractograms, which should be around 1.4 for NCM cathode materials with high capacity.[11,77,81,82] Values below 1.4 are interpreted as evidence for cation mixing, namely a displacement, between Ni^{2+} and Li^+, where the nickel ions occupy sites in the Li^+-ion layer. The higher the degree of displacement the weaker the intensity of the 003 reflection while the 104 reflection remains unaffected.[82] The second quality criterion is the so-called R value, the ratio between the integrated intensities of the combined 006 and 102 reflections to the 101 one. This value is a measure for the hexagonal ordering and should be as small as possible.[81,83] In Table 2 both values are given for the NCM materials.

The rather low values for I_{003}/I_{104} and the very high values for R suggest a high degree of cation mixing in our NCM materials, which increases with the increased Ni content. The cation mixing leads to blocking of mobile Li^+-ions that cannot further participate in the lithium extraction/insertion. This conclusion is further confirmed by galvanostatic measurements at different current densities (Figure 7 a) and long-time measurements at high current densities (Figure 7 b).

Both measurements show capacities far below expected values for all NCM materials. It is obvious that the lower the ratio between I_{003}/I_{104}, the lower the discharge capacities, which strongly suggests that most of the lithium is blocked by cation mixing. It appears that the synthesis procedure using an intermediate step of cubic rock-salt type pre-NCM favours the cation mixing, as all the metal ions are already equally distributed within the rock-salt lattice. With this in mind, a synthesis *via* hexagonal layered transition metal hydroxides with lithium precursor might be more appropriate route to avoid the cation mixing.[77]

However, even in spite of the unfavorable cation mixing, the obtained NCM nanostructures exhibit very good capacity retention and cycling stability even at extreme high charging
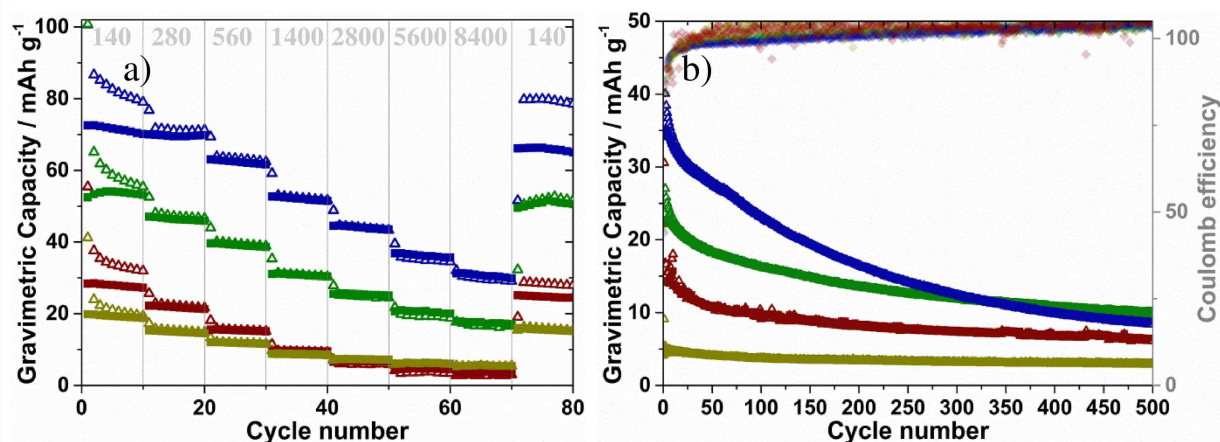
Table 2. Compositions of the as-prepared and the washed nanoparticles of pre-NCMs in comparison. The average nanoparticle sizes calculated from the line broadening in the XRD pattern are given as well.

NCM Material	I_{003}/I_{104}	R
NCM333	1.01	0.83
NCM523	0.74	0.80
NCM613	0.65	0.83
NCM811	0.48	1.46

Figure 7. Electrochemical Li insertion/extraction with NCC-nanostructured NCM333 (blue), NCM523 (green), NCM613 (red) and NCM811 (dark yellow): Rate capabilities at different current densities (140, 280, 560, 1400, 2800, 5600 and 8400 mA g^{-1}) with ten cycles each (a) and long term cyclic performance at 1400 mA g^{-1} showing gravimetric capacity on the left (same symbols as in (a))and Coulomb efficiency (diamond symbols with the same color codes as in (a)) on the right y-axis (b). Open triangular symbols: Li extraction (charging), full square-like symbols: Li insertion (discharging).

and discharging current densities of 5600 mA g^{-1} and 8400 mA g^{-1}. For NCM333 at a charge/discharge current density of 140 mA g^{-1} (corresponding to 1 C, which means the charge/discharge of the full capacity within one hour) only half of the expected capacity is reached with 72 mAh g^{-1}. Nevertheless, with current densities of 5600 mA g^{-1} (40 C, charge/discharge process of 90 s) and 8400 mA g^{-1} (60 C, charge/discharge process of 60 s) 37 mAh g^{-1} and 31 mAh g^{-1}, respectively, can still be achieved. These values are still around 25% and 20%, respectively, of the theoretical expected specific capacity for NCM333. With rising nickel content, we expect an increase in overall theoretical capacity, but here we observe capacity values much lower than those for NCM333.

3. Conclusion

We performed solvothermal reactions of Ni(OAc)$_2$, Co(OAc)$_2$ and Mn(acac)$_2$ in different stoichiometries together with LiOiPr in *tert*-butanol in order to obtain four different compositions of the pseudo-quaternary phase of Li$_w$Ni$_x$Co$_y$Mn$_z$O$_\delta$ ($\delta \leq 1$) (pre-NCM). The Li content was varying between 20–30 at% within the four different crystalline materials, all adopting the cubic rock-salt structure. Here, we describe for the first time the formation of all four pseudo-quaternary phases and were further able to synthesize them as ultrasmall dispersible nanoparticles in the size range of 1–4 nm and at very low temperatures such as 170 °C in a solvothermal environment. These different pre-NCM nanoparticles can be completely transformed into the respective NCM nanoparticles with fixed transition metal ratio by addition of a slightly overstoichiometric amount of lithium precursor at the rather low temperature of 560 °C. Moreover, we were able to obtain NCMs with a desert-rose type interconnected nanoparticle morphology by nanocellulose-mediated calcination of the pre-NCM nanocrystals. The size and the morphology of the NCM nanoparticles strongly depend on the nickel content. The higher the nickel content the smaller and less elongated are the resulting NCM nanoparticles. Furthermore, with rising nickel content an increased mixing of the cations within the NCM phase is observed. This leads to poor capacity retention of the NCMs, especially for NCM631 and NCM811. Nevertheless, in high rate performance tests at charge/discharge times of only 90 s (40 C) or 60 s (60 C) still 25% and 20% of the theoretical capacity of NCM333 can preserved, respectively.

Experimental

Syntheses of Li$_w$Ni$_x$Co$_y$Mn$_z$O$_\delta$ (pre-NCM) nanoparticles: Pure cobalt(II) acetate tetrahydrate (Co(OAc)$_2$) was purchased from AppliChem, nickel(II) acetate tetrahydrate (Ni(OAc)$_2$, 98% purity) and pure manganese(II) acetylacetonate (Mn(acac)$_2$) both from Aldrich, pure lithium *iso*-propoxide (LiOiPr) from Acros Organics and *tert*-butanol from VWR Chemicals (100% purity). All chemicals were used as received.

For the syntheses of the pre-NCM nanoparticles with different compositions, typically, 1.47 mmol (97.1 mg) of LiOiPr was mixed with a total amount of 1.40 mmol of the transition metal compounds with ratios according to the desired final composition of NCM. Hereby, in all formulations LiOiPr is added in excess of 5% to the necessary stoichiometric amount. For example, for NCM811 279.0 mg (1.12 mmol) of Ni(OAc)$_2$, 35.4 mg (0.14 mmol) of Co(OAc)$_2$ and 34.8 mg (0.14 mmol) of Mn(acac)$_2$ are weighed in together with LiOiPr. All metal salts were then dispersed in 180 mL *tert*-butanol in a Parr Instruments 300 mL General Purpose & High Temperature Pressure Vessel steel autoclave with internal temperature and pressure sensor. The sealed autoclave was heated at 10 °C min^{-1} to 165 °C and kept there for 17 h. During this time, the reaction dispersion was stirred at 1000 rpm. After cooling down to room temperature with an approximately cooling rate of 2 °C min^{-1}, the different pre-NCM nanoparticles were collected by simply drying the processed dispersion at 70 °C. For the preparation of stock dispersions of the pre-NCM nanoparticles, 100 mg of the as-prepared and dried solid was wetted with 200 mg, for pre-NCM811 with 400 mg acetic acid. Afterwards, 4 mL of ethanol was added to all dispersions, which were then stirred for two days. Afterwards, remaining agglomerates were removed by filtration with a 220 nm syringe filter (Sartorius minisart cellulose acetate membrane) For DLS measurements, the dispersions were diluted at a ratio of 1:50 with ethanol.

For TEM measurements, the as-prepared pre-NCM solids were washed with ethanol, subsequently centrifuged for 15 min at 50000 rcf (relative centrifugal force) and the supernatant solutions removed. The remaining powders were again dried at 70 °C in air.

Extraction of cellulose nanocrystals: For the extraction of nano-crystalline cellulose, cotton linters CP20 (Peter Temming AG) were hydrolyzed in concentrated sulfuric acid.[84] The linters were washed with water and dried at 60 °C. 1 mL of 64% H$_2$SO$_4$ was added to 8.75 g cellulose fibers, letting the linters soak in the acid for 25 min at room temperature. Thereafter, the mixture was heated to 55 °C for 45 min under vigorous stirring. Hereby, large cellulose aggregates dissolved. Afterwards, the suspension was diluted with 10 times the volume of deionized water and kept in this stage overnight. The formed supernatant was decanted and the NCC-rich phase on the bottom was washed three times with water and subsequently centrifugated at 50000 rcf for 15 min. The last centrifugation step was performed at 70 rcf for 10 min to remove sedimented cellulose aggregates and to collect the NCC dispersion. In the end, the dispersion was concentrated in a rotary evaporator to a stock solution with 6.2 wt% NCC at pH 2.55.[69]

Fabrication of NCC-templated NCMs: For the preparation of NCC-templated NCM material, 1 mL of the filtered pre-NCM dispersion was diluted with 1.697 mL deionized water and mixed with 0.403 mL of the NCC stock solution under vigorous stirring for 5 min. 1.25 mL of the resulting suspension with an NCC content of 0.8 wt% was drop-cast on a 6 cm × 6 cm fluorine doped tin oxide (FTO) glass substrate, dried at 60 °C in an oven and afterwards heated up to 560 °C with a heating rate of 3 °C min^{-1}. The dwell time of the calcination under air was 5 h and the FTO glass substrates were immediately cooled down to room temperature on a stainless-steel rack. The NCC nanostructured NCM was scratched off the FTO glass using stainless-steel razor blades and used for further characterization and processing.

NCM compound electrode preparation: NCC nanostructured NCM powders were mixed together with carbon black Super C65 (TIMCAL) and poly(vinylidene fluoride) (PVdF) from Aldrich in a ratio of 80:10:10, respectively. 1-methyl-2-pyrrolidinone (Sigma-Aldrich, 99% purity) was added in the ratio of 3.7 μL:1 mg of the composite mixture. The inks were all stirred overnight, vortexed thoroughly for 10 min (Vortex Mixer ZX3 of fisherbrand) and treated for 30 min with an ultrasonic horn (Sonopuls GM 4100 of Bandelin) at half

power. Wet films of the ink with a thickness of 100 µm were coated on aluminum foil with an automatic film applicator coater ZAA 2300 from Zehntner with a coating speed of 7 mm s^{-1} and dried afterwards at 60 °C for 3 h. Circular electrodes of 18 mm in diameter were punched out and then dried at 120 °C for 5 h under vacuum. The average active mass loading was 0.5 mg cm^{-2}.

Materials characterization: Wide angle X-ray diffraction analysis of the powders was performed in transmission mode (Debye-Scherrer geometry) using a STOE STADI P diffractometer with a Ge(111) single crystal monochromator for Cu-K$_{\alpha 1}$ ($\lambda = 1.54060$ Å) equipped with a DECTRIS solid state strip detector MYTHEN 1 K.

Raman spectra were acquired with a Jobin Yvon Horiba HR800 UV Raman microscope (OLYMPUS BX41) using a HeNe laser (632.8 nm) and a SYMPHONY CCD detection system. Spectra were recorded using a lens with a 10-fold magnification. The power of the laser beam was normally adjusted to about 8.5 mW.

Scanning electron microscopy (SEM) was carried out on a JEOL JSM-6500F scanning electron microscope equipped with a field emission gun operating at 5 kV and a FEI Helios NanoLab G3 UC scanning electron microscope equipped with a field emission gun usually operated at 3 kV. The films were prepared on FTO glass substrates and glued onto a brass sample holder with silver lacquer.

(S)TEM analysis was carried out on a probe corrected FEI Titan Themis 300 instrument equipped with a field emission gun operating at 300 kV, a high-angle annular dark-field (HAADF) detector, a Super-X energy-dispersive X-ray spectrometer and a Gatan Enfinium ER/977EELS spectrometer. The washed pre-NCM nanoparticles were drop-coated from strongly diluted dispersions on a copper grid with a holey carbon film. NCM materials were scratched off the FTO substrate, wetted with ethanol and deposited on the same type of copper grid. To determine the ratio of transition metals in single nanoparticles, spectrum images were recorded at a convergence angle of 17 mrad and integrated. The L$_{2,3}$ edge signals of the transition metals were extracted by background fitting to a power law function and using energy offsets of 20 eV and energy windows of 50 eV. For quantification, Hartree-Slater scattering cross sections were used.

Dynamic light scattering (DLS) of the pre-NCM nanoparticles was performed using a Malvern Zetasizer-Nano with a 4 mW He—Ne laser (633 nm) and an avalanche photodiode detector. The scattering data were evaluated based on particle number.

Thermogravimetric analysis (TGA) and differential scanning calorimetry (DSC) was carried out with a NETZSCH STA 440 C TG/DSC instrument (heating rate 10 K min^{-1} in a stream of synthetic air of about 25 mL min^{-1}).

Inductively coupled plasma optical emission spectroscopy was performed on a VARIAN VISTA RL CCD Simultaneous ICP-OES.

XPS analyses of the washed and calcined particles were performed with the non-monochromatized Mg-K$_\alpha$ radiation of a VSW TA10 X-ray source (Mg-K$_\alpha = 1253.6$ eV) and a VSW HA100 electron analyzer. Fitting of the Co2p$_{3/2}$ peaks was based on a convolution of a Doniach-Šunjić-function and a Gaussian function with a linear background subtraction. To eliminate peak shifts due to charging of the nanoparticles the carbon 1 s peak was calibrated to 284.5 eV. Determination of the chemical state of Co, Ni and Mn is based on fit parameters published by Biesinger *et al.*.[58] For the XPS measurements the particles were drop-cast on a gold-coated silicon substrate.

^{7}Li magic angle spinning solid state nuclear magnetic resonance (MAS-NMR) spectra were recorded on a Bruker DSX Avance 500 FT spectrometer with a magnetic field of 11.7 T. The zirconia rotor with an outer diameter of 2.5 mm was spun at a rotation frequency of 12 kHz.

Nitrogen sorption measurements were performed at 77 K with the scratched-off powder of nanostructured NCM materials using a QUANTACHROME Autosorb iQ instrument. The powders were degassed at 120 °C for at least 12 h before measurement. The specific surface area was determined with the Brunauer-Emmett-Teller method. The pore size distribution was calculated using a non-local density functional theory (NLDFT) approach for silica cylindrical pores.

Electrochemical Measurements: Electrochemical measurements were performed in an EL-CELL ECC-PAT-Core three-electrode setup using an Autolab potentiostat/galvanostat PGSTAT302 N with FRA32 M module operating with Nova 1.10.4 software. The NCM compound electrodes were separated from the Li metal foil anode by an insulation sleeve equipped with a WHATMAN glass-fiber separator and a lithium metal reference ring. We used the commercial electrolyte PuriEL 1.15 M LiPF$_6$ in ethylene carbonate (EC)/ethyl-methyl-carbonate (EMC)/dimethylcarbonate (DMC) in a 2:2:6 volume to volume ratio and 1.0 wt% fluoroethylene carbonate (FEC) purchased from Soulbrain MI.

Cyclic voltammetry measurements were usually performed between 3 V and 4.3 V vs. Li/Li$^+$ and with a scan speed of 0.5 mV s^{-1}.

Galvanostatic measurements were performed using off voltages of 3 V and 4.3 V vs. Li/Li$^+$, respectively. Both charge and discharge steps were performed at the same current density. A potentiostatic step at 4.3 V was performed between the galvanostatic charge and discharge steps until the charge/discharge current density was reached.

Supporting Information

Supporting Information is available from the Wiley Online Library or from the author.

Acknowledgements

Conflict of Interest

The authors declare no conflict of interest.

[1] K. Mizushima, P. C. Jones, P. J. Wiseman, J. B. Goodenough, *Mater. Res. Bull.* **1980**, *15*, 783.
[2] K. Ozawa, *Solid State Ionics* **1994**, *69*, 212.

[3] G. E. Blomgren, *J. Electrochem. Soc.* **2017**, *164*, A5019.

[4] M. Ma, N. A. Chernova, B. H. Toby, P. Y. Zavalij, M. S. Whittingham, *J. Power Sources* **2007**, *165*, 517.

[5] M. Sathiya, G. Rousse, K. Ramesha, C. P. Laisa, H. Vezin, M. T. Sougrati, M. L. Doublet, D. Foix, D. Gonbeau, W. Walker, A. S. Prakash, M. Ben Hassine, L. Dupont, J. M. Tarascon, *Nat. Mater.* **2013**, *12*, 827.

[6] Y. Wang, J. Jiang, J. R. Dahn, *Electrochem. Commun.* **2007**, *9*, 2534.

[7] J. W. Fergus, *J. Power Sources* **2010**, *195*, 939.

[8] X. Xu, S. Lee, S. Jeong, Y. Kim, J. Cho, *Mater. Today* **2013**, *16*, 487.

[9] Y. Tang, Y. Zhang, W. Li, B. Ma, X. Chen, *Chem. Soc. Rev.* **2015**, *44*, 5926.

[10] M. Park, X. Zhang, M. Chung, G. B. Less, A. M. Sastry, *J. Power Sources* **2010**, *195*, 7904.

[11] K. M. Shaju, G. V. Subba Rao, B. V. R. Chowdari, *Electrochim. Acta* **2002**, *48*, 145.

[12] S. H. Kang, J. Kim, M. E. Stoll, D. Abraham, Y. K. Sun, K. Amine, *J. Power Sources* **2002**, *112*, 41.

[13] J. M. Szeifert, J. M. Feckl, D. Fattakhova-Rohlfing, Y. Liu, V. Kalousek, J. Rathousky, T. Bein, *J. Am. Chem. Soc.* **2010**, *132*, 12605.

[14] J. M. Feckl, K. Fominykh, M. Döblinger, D. Fattakhova-Rohlfing, T. Bein, *Angew. Chem. Int. Ed.* **2012**, *51*, 7459.

[15] F. Zoller, K. Peters, P. M. Zehetmaier, P. Zeller, M. Döblinger, T. Bein, Z. k Sofer, D. Fattakhova-Rohlfing, *Adv. Funct. Mater.* **2018**, *28*, 1706529.

[16] P. M. Zehetmaier, A. Cornélis, F. Zoller, B. Boeller, A. Wisnet, M. Döblinger, D. Boehm, T. Bein, D. Fattakhova-Rohlfing, *Chem. Mater.* **2019**, *31*, 8685.

[17] Z.-D. Huang, X.-M. Liu, S.-W. Oh, B. Zhang, P.-C. Ma, J.-K. Kim, *J. Mater. Chem.* **2011**, *21*, 10777.

[18] C. Yang, J. Huang, L. Huang, G. Wang, *J. Power Sources* **2013**, *226*, 219.

[19] C. Li, Q. Hou, S. Li, F. Tang, P. Wang, *J. Alloys Compd.* **2017**, *723*, 887.

[20] X.-M. Liu, W.-L. Gao, B.-M. Ji, *J. Sol-Gel Sci. Technol.* **2012**, *61*, 56.

[21] K. Myoujin, T. Ogihara, N. Ogata, K. Nakane, T. Kodera, S. Omura, M. Uede, K. Higeta, *Key Eng. Mater.* **2006**, *320*, 255.

[22] J. Zhu, K. Yoo, A. Denduluri, W. Hou, J. Guo, D. Kisailus, *J. Mater. Res.* **2014**, *30*, 286.

[23] F. Wu, M. Wang, Y. Su, L. Bao, S. Chen, *J. Power Sources* **2010**, *195*, 2362.

[24] J. Xie, X. Huang, Z. Zhu, J. Dai, *Ceram. Int.* **2010**, *36*, 2485.

[25] C.-H. Lu, Y.-K. Lin, *J. Power Sources* **2009**, *189*, 40.

[26] S. Patoux, M. M. Doeff, *Electrochem. Commun.* **2004**, *6*, 767.

[27] W. D. Johnston, R. R. Heikes, D. Sestrich, *J. Phys. Chem. Solids* **1958**, *7*, 1.

[28] J. van Elp, J. Wieland, H. Eskes, P. Kuiper, G. Sawatzky, F. de Groot, T. Turner, *Phys. Rev. B* **1991**, *44*, 6090.

[29] M. Antaya, K. Cearns, J. S. Preston, J. N. Reimers, J. R. Dahn, *J. Appl. Phys.* **1994**, *76*, 2799.

[30] E. Iguchi, T. Hashimoto, S. Yokoyama, *J. Phys. Soc. Jpn.* **1996**, *65*, 221.

[31] E. Antolini, *Int. J. Inorg. Mater.* **2001**, *3*, 721.

[32] Y. Wu, D. Pasero, E. E. McCabe, Y. Matsushima, A. R. West, *J. Mater. Chem.* **2009**, *19*, 1443.

[33] J. B. Goodenough, D. G. Wickham, W. J. Croft, *J. Phys. Chem. Solids* **1958**, *5*, 107.

[34] S. Van Houten, *J. Phys. Chem. Solids* **1960**, *17*, 7.

[35] J. C. Danko, G. R. Kilp, H. M. Ferrari, *Solid-State Electron.* **1961**, *3*, 233.

[36] W. Bronger, H. Bade, W. Klemm, *Z. Anorg. Allg. Chem.* **1964**, *333*, 188.

[37] P. Kuiper, G. Kruizinga, J. Ghijsen, G. A. Sawatzky, H. Verweij, *Phys. Rev. Lett.* **1989**, *62*, 221.

[38] V. Berbenni, V. Massarotti, D. Capsoni, R. Riccardi, A. Marini, E. Antolini, *Solid State Ionics* **1991**, *48*, 101.

[39] W. Li, J. N. Reimers, J. R. Dahn, *Phys. Rev. B* **1992**, *46*, 3236.

[40] J. van Elp, H. Eskes, P. Kuiper, G. A. Sawatzky, *Phys. Rev. B* **1992**, *45*, 1612.

[41] Z. Li, C. Wang, X. Ma, L. Yuan, J. Sun, *Mater. Chem. Phys.* **2005**, *91*, 36.

[42] S. Holgersson, A. Karlsson, *Z. Anorg. Allg. Chem.* **1929**, *182*, 255.

[43] Y. J. Mai, J. P. Tu, X. H. Xia, C. D. Gu, X. L. Wang, *J. Power Sources* **2011**, *196*, 6388.

[44] G. Natu, P. Hasin, Z. Huang, Z. Ji, M. He, Y. Wu, *ACS Appl. Mater. Interfaces* **2012**, *4*, 5922.

[45] W. Du, Y. Gao, Q. Tian, D. Li, Z. Zhang, J. Guo, X. Qian, *J. Nanopart. Res.* **2015**, *17*, 368.

[46] T. V. Thi, A. K. Rai, J. Gim, J. Kim, *J. Power Sources* **2015**, *292*, 23.

[47] K. Fominykh, G. C. Tok, P. Zeller, H. Hajiyani, T. Miller, M. Döblinger, R. Pentcheva, T. Bein, D. Fattakhova-Rohlfing, *Adv. Funct. Mater.* **2017**, *27*, 1605121.

[48] C. A. Barrett, E. B. Evans, *J. Am. Ceram. Soc.* **1964**, *47*, 533.

[49] W. Wei, W. Chen, D. G. Ivey, *Chem. Mater.* **2008**, *20*, 1941.

[50] E. McCalla, J. R. Dahn, *Solid State Ionics* **2013**, *242*, 1.

[51] J. M. Szeifert, D. Fattakhova-Rohlfing, D. Georgiadou, V. Kalousek, J. Rathouský, D. Kuang, S. Wenger, S. M. Zakeeruddin, M. Grätzel, T. Bein, *Chem. Mater.* **2009**, *21*, 1260.

[52] Y. Liu, J. M. Szeifert, J. M. Feckl, B. Mandelmeier, J. Rathousky, O. Hayden, D. Fattakhova-Rohlfing, T. Bein, *ACS Nano* **2010**, *4*, 5373.

[53] K. Fominykh, J. M. Feckl, J. Sicklinger, M. Döblinger, S. Böcklein, J. Ziegler, L. Peter, J. Rathousky, E.-W. Scheidt, T. Bein, D. Fattakhova-Rohlfing, *Adv. Funct. Mater.* **2014**, *24*, 3123.

[54] Y. Liu, K. Peters, B. Mandlmeier, A. Müller, K. Fominykh, J. Rathousky, C. Scheu, D. Fattakhova-Rohlfing, *Electrochim. Acta* **2014**, *140*, 108.

[55] J. M. Feckl, H. K. Dunn, P. M. Zehetmaier, A. Müller, S. R. Pendlebury, P. Zeller, K. Fominykh, I. Kondofersky, M. Döblinger, J. R. Durrant, C. Scheu, L. Peter, D. Fattakhova-Rohlfing, T. Bein, *Adv. Mater. Interfaces* **2015**, *2*, 1500358.

[56] K. Fominykh, P. Chernev, I. Zaharieva, J. Sicklinger, G. Stefanic, M. Döblinger, A. Müller, A. Pokharel, S. Böcklein, C. Scheu, T. Bein, D. Fattakhova-Rohlfing, *ACS Nano* **2015**, *9*, 5180.

[57] K. Peters, P. Zeller, G. Stefanic, V. Skoromets, H. Němec, P. Kužel, D. Fattakhova-Rohlfing, *Chem. Mater.* **2015**, *27*, 1090.

[58] M. C. Biesinger, B. P. Payne, A. P. Grosvenor, L. W. M. Lau, A. R. Gerson, R. S. C. Smart, *Appl. Surf. Sci.* **2011**, *257*, 2717.

[59] B. Rivas-Murias, V. Salgueiriño, *J. Raman Spectrosc.* **2017**, *48*, 837.

[60] N. Mironova-Ulmane, A. Kuzmin, M. Grube, *J. Alloys Compd.* **2009**, *480*, 97.

[61] N. Mironova-Ulmane, A. Kuzmin, I. Steins, J. Grabis, I. Sildos, M. Pärs, *J. Phys. Conf. Ser.* **2007**, *93*, 012039.

[62] L. D. L. S. Valladares, A. Ionescu, S. Holmes, C. H. W. Barnes, A. B. Domínguez, O. A. Quispe, J. C. González, S. Milana, M. Barbone, A. C. Ferrari, H. Ramos, Y. Majima, *J. Vac. Sci. Technol. B* **2014**, *32*, 051808.

[63] K. Ramesh, L. Chen, F. Chen, Y. Liu, Z. Wang, Y.-F. Han, *Catal. Today* **2008**, *131*, 477.

[64] J. B. Wang, G. J. Huang, X. L. Zhong, L. Z. Sun, Y. C. Zhou, E. H. Liu, *Appl. Phys. Lett.* **2006**, *88*, 252502.

[65] S. Muto, K. Tatsumi, *Microscopy* **2017**, *66*, 39.

[66] Y. Habibi, L. A. Lucia, O. J. Rojas, *Chem. Rev.* **2010**, *110*, 3479.

[67] A. Dufresne, *Mater. Today* **2013**, *16*, 220.

[68] A. Ivanova, D. Fattakhova-Rohlfing, B. E. Kayaalp, J. Rathouský, T. Bein, *J. Am. Chem. Soc.* **2014**, *136*, 5930.

[69] A. Ivanova, K. Fominykh, D. Fattakhova-Rohlfing, P. Zeller, M. Döblinger, T. Bein, *Inorg. Chem.* **2015**, *54*, 1129.

[70] A. Ivanova, M. C. Fravventura, D. Fattakhova-Rohlfing, J. Rathouský, L. Movsesyan, P. Ganter, T. J. Savenije, T. Bein, *Chem. Mater.* **2015**, *27*, 6205.

[71] E. Dujardin, M. Blaseby, S. Mann, *J. Mater. Chem.* **2003**, *13*, 696.

[72] D. Klemm, F. Kramer, S. Moritz, T. Lindström, M. Ankerfors, D. Gray, A. Dorris, *Angew. Chem. Int. Ed.* **2011**, *50*, 5438.

[73] C. Julien, *Solid State Ionics* **2000**, *136–137*, 887.

[74] M. Inaba, Y. Iriyama, Z. Ogumi, Y. Todzuka, A. Tasaka, *J. Raman Spectrosc.* **1997**, *28*, 613.

[75] S.-J. Hwang, H.-S. Park, J.-H. Choy, G. Campet, J. Portier, C.-W. Kwon, J. Etourneau, *Electrochem. Solid-State Lett.* **2001**, *4*, A213.

[76] A. M. Hashem, R. S. El-Taweel, H. M. Abuzeid, A. E. Abdel-Ghany, A. E. Eid, H. Groult, A. Mauger, C. M. Julien, *Ionics* **2012**, *18*, 1.

[77] L. -j Li, X. -h Li, Z. -x Wang, H. -j Guo, P. Yue, W. Chen, L. Wu, *Powder Technol.* **2011**, *206*, 353.

[78] H.-J. Noh, S. Youn, C. S. Yoon, Y.-K. Sun, *J. Power Sources* **2013**, *233*, 121–130.

[79] S.-K. Jung, H. Gwon, J. Hong, K.-Y. Park, D.-H. Seo, H. Kim, J. Hyun, W. Yang, K. Kang, *Adv. Energy Mater.* **2014**, *4*, 1300787.

[80] C. Zhang, M. Liu, G. Pan, S. Liu, D. Liu, C. Chen, J. Su, T. Huang, A. Yu, *ACS Appl. Energy Mater.* **2018**, *1*, 4374.

[81] T. Ohzuku, A. Ueda, M. Nagayama, *J. Electrochem. Soc.* **1993**, *140*, 1862.

[82] T. Ohzuku, A. Ueda, M. Nagayama, Y. Iwakoshi, H. Komori, *Electrochim. Acta* **1993**, *38*, 1159.

[83] J. R. Dahn, U. von Sacken, C. A. Michal, *Solid State Ionics* **1990**, *44*, 87.

[84] X. M. Dong, T. Kimura, J.-F. Revol, D. G. Gray, *Langmuir* **1996**, *12*, 2076.